

# Image reconstruction from fan-beam projections on less than a short scan

Frédéric Noo<sup>1</sup>, Michel Defrise<sup>2</sup>, Rolf Clackdoyle<sup>1</sup> and Hiroyuki Kudo<sup>3</sup>

<sup>1</sup> Department of Radiology, University of Utah, Salt Lake City, UT, USA

<sup>2</sup> Division of Nuclear Medicine, Vrije Universiteit of Brussels, Brussels Belgium

<sup>3</sup> Institute of Information Sciences and Electronics, University of Tsukuba, Tsukuba, Japan

E-mail: noo@doug.med.utah.edu

Received 17 January 2002

Published 4 July 2002

Online at [stacks.iop.org/PMB/47/2525](http://stacks.iop.org/PMB/47/2525)

## Abstract

This work is concerned with 2D image reconstruction from fan-beam projections. It is shown that exact and stable reconstruction of a given region-of-interest in the object does not require all lines passing through the object to be measured. Complete (non-truncated) fan-beam projections provide sufficient information for reconstruction when ‘every line passing through the region-of-interest intersects the vertex path in a non-tangential way’. The practical implications of this condition are discussed and a new filtered-backprojection algorithm is derived for reconstruction. Experiments with computer-simulated data are performed to support the mathematical results.

## 1. Introduction

This paper presents new results for two-dimensional (2D) image reconstruction from fan-beam projections in x-ray computed tomography (CT). To simplify the exposition, the data acquisition geometry is described using the general terms *vertex point* and *vertex path*. The vertex point is the converging point of the line integrals in a fan-beam projection, and the vertex path is the trajectory along which the projections are measured. The vertex point corresponds to the position of the x-ray source in CT, and the vertex path is usually a circle or a circular arc. An overview of the principles of CT imaging can be found in Kak and Slaney (1987).

For 2D image reconstruction, it is generally believed that accurate and stable reconstruction of any region-of-interest (ROI) requires the line integrals of the object density to be known for all lines passing through the object. When applied to fan-beam data acquisition on a circular trajectory, this condition leads to the notion of circular short-scan. Consider that the object is confined in a disc of radius  $R_m$  and the vertex point moves on a circle of radius  $R_o$  centred on that disc. In this case, the detector extent must be large enough to subtend the fan-angle of  $\pm\gamma_m = \pm\arcsin(R_m/R_o)$  in order to avoid truncated fan-beam projections, and the vertex must travel on a continuous arc of  $\pi + 2\gamma_m$  to ensure that all lines

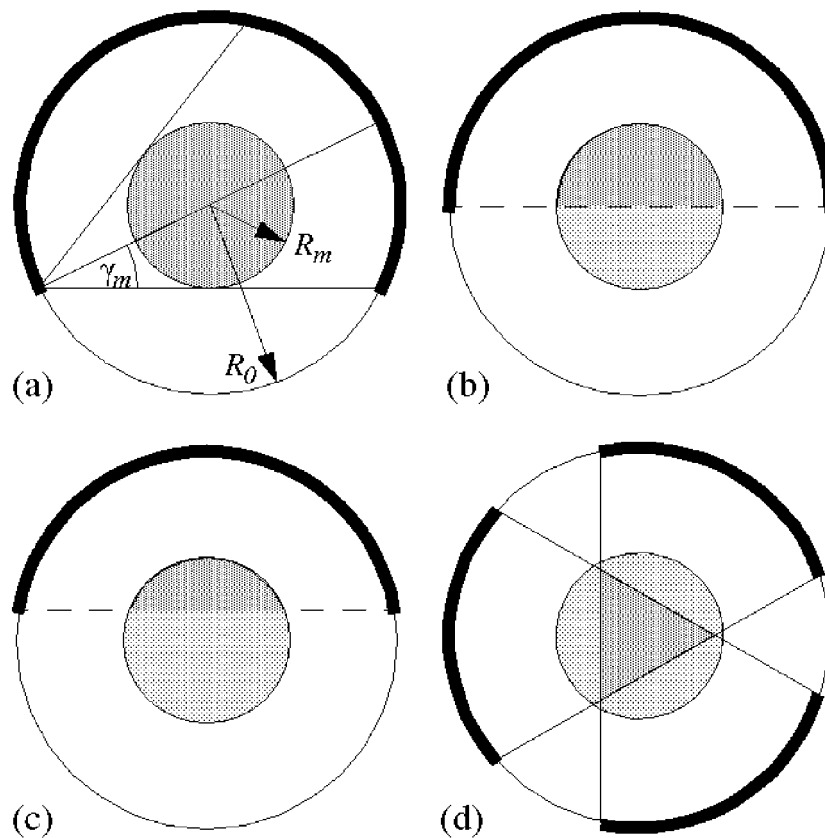


**Figure 1.** Short-scan and three very short-scans. The object is assumed to occupy the circular shaded region of radius  $R_m$ , and the vertex path lies on a concentric circle of radius  $R_o$ . The detector is always large enough to image the full object, thereby accommodating a maximum fan-angle of  $\gamma_m$ . (a) A conventional short-scan of  $\pi + 2\gamma_m$  allows reconstruction of the whole object. (b)–(c) A continuous scan of less than  $\pi + 2\gamma_m$  allows reconstruction of all object points inside the convex hull of the scan. (d) A scan of three equally spaced segments of  $80^\circ$  each allows reconstruction of a triangular ROI in the centre of the object.

passing through the disc of radius  $R_m$  are measured (see figure 1(a)). In the literature, the range  $\pi + 2\gamma_m$  is referred to as a short scan.

In this paper, it is shown that the short-scan condition can usually be relaxed if only an ROI inside the object needs to be reconstructed. More generally, it is shown that 2D reconstruction of a given ROI inside an object can be achieved from fan-beam projections if (i) the *object* is not truncated in any of the required fan-beam projections, and (ii) all lines through the ROI are measured. The second requirement invokes conditions on the locations of the vertex points, and for circular scanning it is the reduced requirement of the ROI (rather than the object) which relaxes the short-scan condition. For example, it is shown that complete (non-truncated) fan-beam projections on a continuous (connected) arc provide enough information for reconstruction at all points within the convex hull of the arc, whether or not the object extends outside that region. See figures 1(b) and (c) for an illustration with an arc of  $180^\circ$  and an arc of  $160^\circ$ , respectively. Small central ROIs can be reconstructed by using several short arcs such as illustrated in figure 1(d) with three equally spaced arcs of length  $80^\circ$  each. For this path, reconstruction is possible for any ROI inside the central triangular region obtained

by joining the beginning point of each arc with the end point of the next arc. In both of these examples, all lines through the ROI are measured but there are some unmeasured lines through the object. It is always assumed, however, that the *object* is not truncated in the projections.

The results of this paper contradict the widespread belief that 2D image reconstruction of an ROI in an object requires knowledge of all the line integrals passing through that object. This belief has been supported by the form of the well-known filtered-backprojection (FBP) formula for 2D parallel-beam reconstruction. However, it should be realized that this formula was derived as a global reconstruction method and no result appears in the literature stating that reconstruction of an ROI from line integrals requires as much data as a global (full object) reconstruction. For ROI reconstruction using conventional FBP, indeed, all line integral measurements through the object are required. However, the fan-beam results presented here will demonstrate that fewer measurements are necessary.

The organization of the paper is as follows. The problem of 2D image reconstruction from parallel-beam projections is reviewed in section 2. In section 3, the discussion moves to reconstruction from fan-beam projections. The link between the Hilbert transform of the projections and the 2D Radon transform of the object is made and a new data completeness condition is stated for reconstruction of a given ROI. This condition is conceptually similar to Tuy's condition for 3D image reconstruction from cone-beam projections (Tuy 1983). Section 4 discusses two different approaches to developing reconstruction algorithms. In the first approach, the fan-beam data are rebinned into the samples of the Hilbert transform of the 2D Radon transform of object density, and reconstruction is achieved subsequently using a variant of standard FBP for parallel-beam reconstruction. This approach is similar to cone-beam tomographic reconstruction using the Grangeat formula (Grangeat 1991) for rebinning and the 3D radon transform for subsequent reconstruction (see, e.g. Noo *et al* 1997). The second approach is more direct and can be seen as a new FBP formula for fan-beam reconstruction. It was inspired by the algorithms for cone-beam spiral CT recently proposed by Katsevich (2002), and can be seen as the fan-beam counterpart of the CB-FBP algorithm of Defrise and Clack (1994) and Kudo and Saito (1994). The new fan-beam FBP formula is given in a very general framework, disregarding the detector geometry. Section 5 shows how to apply this formula for reconstruction from fan-beam projections with equi-angular rays or equally spaced collinear detectors with circular vertex paths. Finally, section 6 presents FBP reconstruction results obtained from computer-simulated data of a head phantom and section 7 discusses some practical implications of the results presented in this paper.

## 2. Parallel-beam geometry

This section gives a brief review of 2D image reconstruction from parallel-beam projections. The discussion is restricted to results which are directly relevant to the rest of the paper.

### 2.1. Notation

In this paper, the 2D object density to be reconstructed is either denoted as  $f$ ,  $f(\underline{x})$  or  $f(x, y)$  with  $\underline{x} = (x, y)$ , according to the context. The parallel-beam projections of  $f$  are given by the expression

$$p(\underline{n}, s) = \int_{\mathbb{R}^2} d\underline{x} f(\underline{x}) \delta(\underline{x} \cdot \underline{n} - s) \quad (1)$$

where  $s \in \mathbb{R}$ ,  $\underline{n}$  is any unit vector and  $\delta$  is the Dirac delta function. In equation (1), the delta function selects values of  $\underline{x}$  that satisfy  $\underline{x} \cdot \underline{n} = s$ , so  $p(\underline{n}, s)$  is the integral of  $f$  on the line

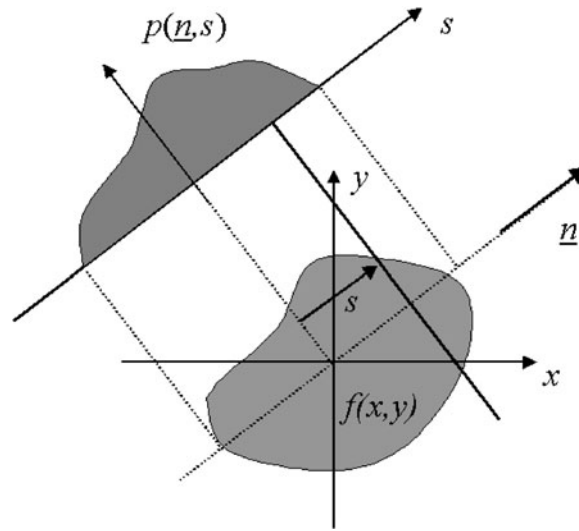


**Figure 2.** Illustration of different parameters appearing in the definition of the parallel-beam projections.

perpendicular to  $\underline{n}$  at the signed distance  $s$  from the origin  $\underline{x} = 0$  as shown in figure 2. The function  $p$  is the Radon transform of  $f$ .

## 2.2. Reconstruction from parallel-beam projections

There exist numerous ways to reconstruct  $f$  from its Radon transform  $p$ . For a good overview, see Kak and Slaney (1987), Natterer (1986), and Natterer and Wübbeling (2001). Only FBP reconstruction algorithms are discussed below.

As is well known, the FBP reconstruction of  $f$  at  $\underline{x}$  from  $p$  proceeds in two steps. In the first step, the projections  $p(\underline{n}, s)$  are filtered in  $s$  to obtain some filtered projections  $p_F(\underline{n}, s)$ . Next,  $f(\underline{x})$  is obtained by adding the values of  $p_F(\underline{n}, s)$  corresponding to lines passing through  $\underline{x}$ . This is the backprojection step. Mathematically,

$$f(\underline{x}) = \int_0^\pi d\phi p_F(\underline{n}, s) \Big|_{s=\underline{x} \cdot \underline{n}} \quad (2)$$

where  $\underline{x} \cdot \underline{n}$  is the scalar product of vectors  $\underline{x}$  and  $\underline{n}$ , and  $\underline{n} = (-\sin\phi, \cos\phi)$ .

The filter to be applied to the projections  $p(\underline{n}, s)$  to obtain  $p_F(\underline{n}, s)$  is the 1D ramp filter

$$h_F(s) = \int_{-\infty}^{+\infty} d\sigma |\sigma| e^{i2\pi\sigma s}. \quad (3)$$

This filter is applied in  $s$  so that

$$p_F(\underline{n}, s) = (h_F * p)(\underline{n}, s) = \int_{\mathbb{R}} ds' h_F(s - s') p(\underline{n}, s'). \quad (4)$$

Because  $|\sigma| = (1/2\pi)(i2\pi\sigma)(-i \operatorname{sign}(\sigma))$ , the application of the ramp filter is equivalent to the successive application of a Hilbert transform and a derivative in  $s$ ,

$$p_F(\underline{n}, s) = \frac{1}{2\pi} \frac{\partial}{\partial s} p_H(\underline{n}, s) \quad (5)$$

where  $p_H(\underline{n}, s)$  is the Hilbert transform of  $p(\underline{n}, s)$  at fixed direction  $\underline{n}$ . Namely,

$$p_H(\underline{n}, s) = (h_H * p)(\underline{n}, s) = \int_{\mathbb{R}} ds' h_H(s - s') p(\underline{n}, s') \quad (6)$$

with

$$h_H(s) = - \int_{-\infty}^{+\infty} d\sigma \, i \operatorname{sign}(\sigma) e^{i2\pi\sigma s}. \quad (7)$$

Using these definitions, the FBP formula (2) can be rewritten in the form

$$f(\underline{x}) = \frac{1}{2\pi} \int_0^\pi d\phi \frac{\partial}{\partial s} p_H(\underline{n}, s) \Big|_{s=\underline{x}\cdot\underline{n}}. \quad (8)$$

Formulae (2) and (8) will be extensively used in the rest of the paper. From these formulae, it is observed that  $f$  can be reconstructed at  $\underline{x}$  provided that either  $p_F(\underline{n}, s)$  is known for all lines passing through  $\underline{x}$  or  $p_H(\underline{n}, s)$  is known for all lines passing through a neighbourhood of  $\underline{x}$  (passing through and near  $\underline{x}$ ). Note that neither the ramp filter nor the Hilbert transform defines a local operation. Therefore, obtaining  $p_F$  or  $p_H$  from formulae (4) or (6) requires the integrals of  $f$  to be known for all lines passing through the support of  $f$ . Formulae for  $p_F$  and  $p_H$  will be given in section 3 that require fewer line integrals of  $f$ .

### 3. Data completeness condition for fan-beam reconstruction

This section discusses the link between fan-beam projections and the Hilbert transform of the 2D Radon transform of  $f$ . This link provides formulae to rebin fan-beam data into samples of  $p_H(\underline{n}, s)$  and  $p_F(\underline{n}, s)$ . From these formulae, new data completeness conditions are derived for ROI fan-beam reconstruction.

#### 3.1. The reconstruction problem

The problem of reconstructing  $f$  from fan-beam projections is investigated for any finite-length vertex path consisting of finitely many smooth (continuously differentiable) curves. The vertex path is parametrized by a scalar  $\lambda$  varying in some interval or union of disjoint intervals  $\Lambda$  of  $\mathbb{R}$ , and the vertex point is  $\underline{a}(\lambda)$ . The vector tangent to the vertex path at  $\underline{a}(\lambda)$  is  $\underline{a}'(\lambda) = d\underline{a}(\lambda)/d\lambda$ . A parametrization can always be found such that  $\underline{a}'(\lambda)$  exists and is non-zero, except at the endpoints of the curves. For example, a semicircle of radius  $R_o$  can be described by the equation  $\underline{a}(\lambda) = (R_o \cos \lambda, R_o \sin \lambda)$  with  $\lambda \in [0, \pi]$ ; in that case,  $\underline{a}'(\lambda) = (-R_o \sin \lambda, R_o \cos \lambda)$  for  $\lambda \in (0, \pi)$ .

The fan-beam projection of  $f$  from the vertex point  $\underline{a}(\lambda)$  is the set of line integrals

$$g(\lambda, \underline{\alpha}) = \int_0^{+\infty} dt f(\underline{a}(\lambda) + t\underline{\alpha}) \quad (9)$$

obtained by varying  $\underline{\alpha}$  in  $S^1$  where  $S^1$  is the set of unit vectors in the  $(x, y)$  plane. Note that equation (9) does not make any assumption about the detector geometry. The particular cases of equi-angular rays and equally spaced collinear detectors are discussed in section 5 as an application of the results presented in this section and the next one. In any case, it is always assumed that the fan-beam projections are non-truncated, i.e.  $g(\lambda, \underline{\alpha})$  is known for all lines diverging from  $\underline{a}(\lambda)$ .

#### 3.2. First rebinning formula

Recall from section 2.2 that  $p_H$  denotes the Hilbert transform of the 2D Radon transform  $p$  of  $f$ . As written in equation (6),  $p_H(\underline{n}, s) = (h_H * p)(\underline{n}, s)$  with  $h_H(s)$  given by equation (7). In appendix A, it is shown that the value of  $p_H$  on any line passing through a vertex point  $\underline{a}(\lambda)$  can be obtained from the fan-beam projection  $g(\lambda, \underline{\alpha})$ . The line  $(\underline{n}, s)$  orthogonal to the unit

vector  $\underline{n}$  and containing  $\underline{a}(\lambda)$  satisfies  $s = \underline{a}(\lambda) \cdot \underline{n}$ . The precise relation for obtaining  $p_H$  on this line is

$$p_H(\underline{n}, s)|_{s=\underline{a}(\lambda)\cdot\underline{n}} = g_H(\lambda, \underline{n}) \quad (10)$$

where

$$g_H(\lambda, \underline{n}) = - \int_{S^1} d\alpha h_H(\underline{n} \cdot \alpha) g(\lambda, \alpha). \quad (11)$$

To appreciate this relation, it is useful to consider the parametrizations

$$\begin{aligned} \alpha &= \alpha(\gamma) = \cos \gamma \underline{e}_1 + \sin \gamma \underline{e}_2 \\ \underline{n} &= \underline{n}(\phi) = -\sin \phi \underline{e}_1 + \cos \phi \underline{e}_2 \end{aligned} \quad (12)$$

where  $\underline{e}_1$  and  $\underline{e}_2$  are two arbitrary unit orthogonal vectors. With these parametrizations and using  $h_H(-s) = -h_H(s)$ , the equation for  $g_H(\lambda, \underline{n})$  appears as a simple convolution:

$$g_H(\lambda, \underline{n}(\phi)) = \int_{-\pi}^{\pi} d\gamma h_H(\sin(\phi - \gamma)) g(\lambda, \alpha(\gamma)). \quad (13)$$

Note that all values of the fan-beam projection  $g(\lambda, \alpha)$  contribute to  $g_H(\lambda, \underline{n})$ , so the projection must not be truncated.

The rebinning formula (10) with  $g_H$  given by (13) (or the more general expression (11)) represents the key result of this paper, from which new data completeness conditions and algorithms for 2D reconstruction are derived below and in the following sections. Equation (10) shows that the calculation of  $p_H$  at  $(\underline{n}, s)$  does not require  $p$  to be known on all lines parallel to the line  $(\underline{n}, s)$ ; this calculation can be made whenever  $p$  is known on the lines that diverge from some point on the line  $(\underline{n}, s)$ . This different orientation of lines in space and the freedom in the selection of the vertex point on the line  $(\underline{n}, s)$  induces new possibilities for 2D reconstruction which are less restrictive than the conventional FBP theory.

Equation (10) provides a new data completeness condition for 2D fan-beam reconstruction. Recall from section 2.2 that  $f$  can be reconstructed at  $\underline{x}$  using a simple backprojection step provided  $p_H$  is known for all lines passing through a neighbourhood of  $\underline{x}$ . Since the rebinning formula (10) states that  $p_H$  is available on all lines that contain a vertex point, the following data completeness condition is obtained.

**Condition 1.** *A region-of-interest can be accurately reconstructed provided every line passing through a neighbourhood of the region-of-interest intersects the vertex path (every such line is a ray in a measured fan-beam projection of the object).*

Throughout this paper, points on the vertex path are not considered to be in an ROI.

The rebinning formula (10) is not new; it is the specific 2D case of an  $n$ -dimensional formula given in Hamaker *et al* (1980), with  $h_H(s)$  replaced by any function  $h(s)$  such that  $h(as) = a^{1-n}h(s)$  for any  $a > 0$ . This general formula has been used to investigate cone-beam reconstruction theory ( $n = 3$ ), but to our knowledge no discussion appears in the literature on its implications for 2D fan-beam reconstruction.

A detailed mathematical proof of equation (10) can be found in Hamaker *et al* (1980). The essential manipulations are repeated in appendix A.

### 3.3. Second rebinning formula

In section 2.2,  $p_F$  was defined as the convolution of  $p$  with the 1D ramp filter. At the end of this section, it is shown that the value of  $p_F$  on any line passing through a vertex point  $\underline{a}(\lambda)$

can be obtained from fan-beam projections with vertices near  $\underline{a}(\lambda)$ . The exact formula to get  $p_F$  on the line containing  $\underline{a}(\lambda)$  and orthogonal to the unit vector  $\underline{n}$  is

$$p_F(\underline{n}, s)|_{s=\underline{a}(\lambda)\cdot\underline{n}} = \frac{1}{2\pi \underline{a}'(\lambda) \cdot \underline{n}} g_F(\lambda, \underline{n}) \quad (14)$$

where

$$g_F(\lambda, \underline{n}) = - \int_{S^1} d\underline{\alpha} h_H(\underline{n} \cdot \underline{\alpha}) g'(\lambda, \underline{\alpha}) \quad (15)$$

with

$$g'(\lambda, \underline{\alpha}) = \frac{\partial}{\partial \lambda} g(\lambda, \underline{\alpha}) = \lim_{\varepsilon \rightarrow 0} \frac{g(\lambda + \varepsilon, \underline{\alpha}) - g(\lambda - \varepsilon, \underline{\alpha})}{2\varepsilon}. \quad (16)$$

The rebinning formula (14) can only hold for non-zero  $\underline{a}'(\lambda) \cdot \underline{n}$ . Therefore, the tangent vector  $\underline{a}'(\lambda)$  must not be orthogonal to  $\underline{n}$ , and equation (14) only applies for vertex points  $\underline{a}(\lambda)$  where the tangent vector  $\underline{a}'(\lambda)$  is not parallel to the line  $(\underline{n}, s)$ .

An important observation is that  $g'(\lambda, \underline{\alpha})$  is the derivative of  $g(\lambda, \underline{\alpha})$  with respect to  $\lambda$  at fixed direction  $\underline{\alpha}$ . This point was emphasized in equation (16). As will be seen in section 5, care must be taken with the definition of  $g'(\lambda, \underline{\alpha})$  when investigating specific detector geometries (see equations (34) and (38)). Note also that unlike  $p_F$ ,  $g_F$  is not simply obtained by ramp filtering the fan-beam projection  $g$ . The Hilbert transform and derivative appearing in equation (15) operate on different variables.

The equation for  $g_F$  can also be written as a convolution, similar to equation (13) for  $g_H$ . The formula is

$$g_F(\lambda, \underline{n}(\phi)) = \int_{-\pi}^{\pi} d\gamma h_H(\sin(\phi - \gamma)) g'(\lambda, \underline{\alpha}(\gamma)) \quad (17)$$

where  $\underline{n}(\phi)$  and  $\underline{\alpha}(\gamma)$  are given by (12).

Recall from section 2.2 that  $f$  can be reconstructed at  $\underline{x}$  using a simple backprojection of the values of  $p_F$  on all lines passing through  $\underline{x}$ . Since the rebinning formula (14) states that  $p_F$  is available on lines that contain certain kinds of vertex points, the following data completeness condition is obtained.

**Condition 2.** *A region-of-interest can be accurately reconstructed provided every line passing through the region-of-interest has a non-tangential and non-endpoint intersection with the vertex path.*

Conditions 1 and 2 only differ in how they express that a small margin is needed. In condition 1, a slightly larger region than the ROI is considered, and for condition 2, a slightly extended vertex path is required instead.

A formal demonstration of formula (14) follows. By definition,

$$g_F(\lambda, \underline{n}) = - \int_{S^1} d\underline{\alpha} h_H(\underline{n} \cdot \underline{\alpha}) \frac{\partial}{\partial \lambda} g(\lambda, \underline{\alpha}) = - \frac{\partial}{\partial \lambda} \int_{S^1} d\underline{\alpha} h_H(\underline{n} \cdot \underline{\alpha}) g(\lambda, \underline{\alpha}) = \frac{\partial}{\partial \lambda} g_H(\lambda, \underline{n}). \quad (18)$$

From the first rebinning formula (equation (10)),

$$\frac{\partial}{\partial \lambda} g_H(\lambda, \underline{n}) = \frac{\partial}{\partial \lambda} (p_H(\underline{n}, \underline{a}(\lambda) \cdot \underline{n})) = (\underline{a}'(\lambda) \cdot \underline{n}) \frac{\partial}{\partial s} p_H(\underline{n}, s) \Big|_{s=\underline{a}(\lambda)\cdot\underline{n}}. \quad (19)$$

Therefore, by combining equations (18), (19) and (5),

$$g_F(\lambda, \underline{n}) = (\underline{a}'(\lambda) \cdot \underline{n}) \frac{\partial}{\partial s} p_H(\underline{n}, s) \Big|_{s=\underline{a}(\lambda)\cdot\underline{n}} = 2\pi (\underline{a}'(\lambda) \cdot \underline{n}) p_F(\underline{n}, s)|_{s=\underline{a}(\lambda)\cdot\underline{n}}. \quad (20)$$

With the assumption that  $\underline{a}'(\lambda) \cdot \underline{n} \neq 0$ , this formula gives the second rebinning formula (equation (14)).

#### 4. Reconstruction algorithms

This section discusses fan-beam reconstruction of a given ROI assuming that the data are complete according to one of the two conditions given in section 3. Two reconstruction approaches are discussed: a rebinning approach that uses formula (10) or (14) to convert from fan-beam geometry to parallel-beam geometry, and an FBP approach that acts sequentially on the fan-beam projections.

##### 4.1. Rebinning methods

The rebinning methods are direct implementations of the rebinning formulae. For the first method, condition 1 is used to identify the required fan-beam projections to reconstruct a specified ROI. These projections are filtered according to equation (13), then rebinned to the parallel-beam geometry using (10). Reconstruction is completed by taking a derivative then backprojecting through the ROI according to equation (8). For the second method, condition 2 is used to identify the required fan-beam projections in terms of the ROI and filtering is performed according to equations (15) and (16). Equation (14) describes the rebinning and reconstruction is completed by backprojecting through the ROI according to equation (2). The only difference in the methods is whether the derivative is performed before or after the rebinning.

Some details on the digital implementation of the first rebinning method are now given. The second method would follow a similar pattern.

To simplify the discussion, the ROI is regarded as a disc of radius  $R_{\text{ROI}}$  and centre  $\underline{x} = 0$ . The fan-beam projections available for reconstruction of that region correspond to a number  $N$  of vertex locations  $\underline{a}(\lambda_i)$ ,  $i = 1, \dots, N$  that sample a vertex path satisfying condition 1.

The ROI is reconstructed using a discretization of the parallel-beam reconstruction formula (8), so a sinogram sampling is first defined with

$$\phi_k = k \frac{\pi}{M} \quad k = 0, \dots, M - 1 \quad (21)$$

and

$$s_l = l \frac{R_{\text{ROI}}}{Q} \quad l = -Q, \dots, Q \quad (22)$$

where  $M \simeq \pi Q$ . Next,  $p_H(\underline{n}(\phi_k), s_l)$  is estimated for each value of  $k$  and  $l$  from the measured projections  $g(\lambda_i, \underline{\alpha})$  using (10) as explained later in this section. Once all  $p_H(\underline{n}(\phi_k), s_l)$  have been estimated,  $p'_H(\underline{n}(\phi_k), s_l) = (\partial p_H / \partial s)(\underline{n}(\phi_k), s_l)$  is computed using the two-point formula

$$p'_H(\underline{n}(\phi_k), s_l) \simeq \frac{p_H(\underline{n}(\phi_k), s_{l+1}) - p_H(\underline{n}(\phi_k), s_{l-1})}{s_{l+1} - s_{l-1}} \quad (23)$$

and  $f(\underline{x})$  is computed according to the formula

$$f(\underline{x}) \simeq \frac{1}{2M} \sum_{k=0}^{M-1} p'_H(\underline{n}(\phi_k), \underline{x} \cdot \underline{n}(\phi_k)) \quad (24)$$

using linear interpolation between the two samples of  $s$  nearest to  $\underline{x} \cdot \underline{n}(\phi_k)$ .

One method for obtaining the value of  $p_H(\underline{n}(\phi_k), s_l)$  from the fan-beam projections would be to directly apply equation (10), i.e. search for the vertex  $\underline{a}(\lambda_i)$  (or vertices if interpolation is used) which minimizes  $|s_l - \underline{a}(\lambda_i) \cdot \underline{n}(\phi_k)|$  and assigns  $g_H(\lambda_i, \underline{n}(\phi_k))$  (or a suitably interpolated value) to  $p_H(\underline{n}(\phi_k), s_l)$ . A much better performance can be achieved, however, by including knowledge of the location of the ROI relative to the vertex path, as suggested by

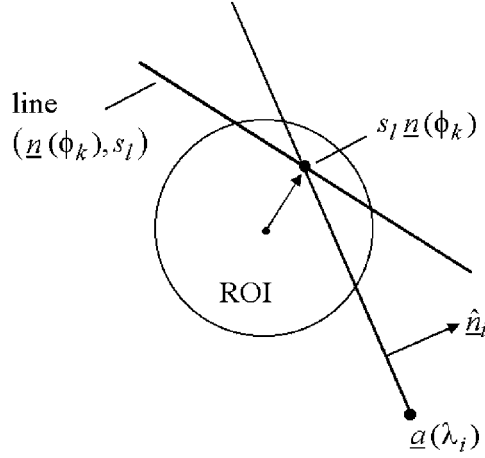


**Figure 3.** Estimate of  $p_F$  on a given line  $(\underline{n}(\phi_k), s_l)$  from the fan-beam projection at  $\underline{a}(\lambda_i)$ . The ROI is viewed as a disc centred at the origin  $\underline{x} = 0$ . The mid-point  $s_l \underline{n}(\phi_k)$  of the intersection of the ROI with the line  $(\underline{n}(\phi_k), s_l)$  is used to define a line containing  $\underline{a}(\lambda_i)$ . Let  $\hat{\underline{n}}_i$  be any unit vector orthogonal to this line. The estimate of  $p_H(\underline{n}(\phi_k), s_l)$  is  $g_H(\lambda_i, \hat{\underline{n}}_i)$ .

Noo *et al* (1997, 1999). Since the ROI is a disc centred at the origin, the point  $s_l \underline{n}(\phi_k)$  is the centre of the line segment formed by the intersection of the ROI with the line  $(\underline{n}(\phi_k), s_l)$  (see figure 3). For each vertex  $\underline{a}(\lambda_i)$ , the line passing through  $\underline{a}(\lambda_i)$  and  $s_l \underline{n}(\phi_k)$  has unit normal denoted  $\hat{\underline{n}}_i$  (mathematically,  $\hat{\underline{n}}_i \cdot (\underline{a}(\lambda_i) - s_l \underline{n}(\phi_k)) = 0$ ). The value assigned to  $p_H(\underline{n}(\phi_k), s_l)$  is  $g_H(\lambda_i, \hat{\underline{n}}_i)$  where  $i$  is such that  $|\hat{\underline{n}}_i \cdot \underline{n}(\phi_k)|$  is maximized over all vertices, or an interpolated value of the form

$$p_H(\underline{n}(\phi_k), s_l) \simeq \sum_{i=1}^N w_i(k, l) g_H(\lambda_i, \hat{\underline{n}}_i(k, l)) \quad (25)$$

where the weights  $w_i(k, l)$  depend on the magnitude of  $\hat{\underline{n}}_i \cdot \underline{n}(\phi_k)$ .

The values of  $g_H(\lambda_i, \hat{\underline{n}}_i(k, l))$  in equation (25) are obtained from the fan-beam projections  $g(\lambda_i, \cdot)$  by an implementation of equation (11). Rather than only calculating  $g_H$  at the required samples  $(\lambda_i, \hat{\underline{n}}_i(k, l))$  it is generally more efficient to convert all projections  $g$  to  $g_H$  using the original discretization scheme and obtain  $g_H(\lambda_i, \hat{\underline{n}}_i(k, l))$  using interpolation in  $(k, l)$ . For equi-angular projections  $g(\lambda_i, \underline{a}(\gamma))$ , the conversion takes the form of a convolution as shown by equation (13), and for equally spaced detector samples it will be readily seen in section 5.2 that equation (11) again reduces to a convolution. Other discretization schemes for the data are not considered here.

#### 4.2. FBP reconstruction

Using equation (14), a fan-beam FBP reconstruction formula is derived in appendix B, assuming that for the given vertex path the ROI satisfies condition 2 given in section 3.3. This FBP formula is

$$f(\underline{x}) = \frac{1}{2\pi} \int_{\Lambda} d\lambda \frac{1}{\|\underline{x} - \underline{a}(\lambda)\|} [w(\lambda, \underline{n}) g_F(\lambda, \underline{n})]_{\underline{n}=\underline{n}^*(\lambda, \underline{x})} \quad (26)$$

for any  $\underline{x}$  in the ROI. The various quantities appearing in this formula are defined as follows. First,  $g_F$  is the filtered fan-beam projection obtained from  $g$  using formulae (15) and (16), and

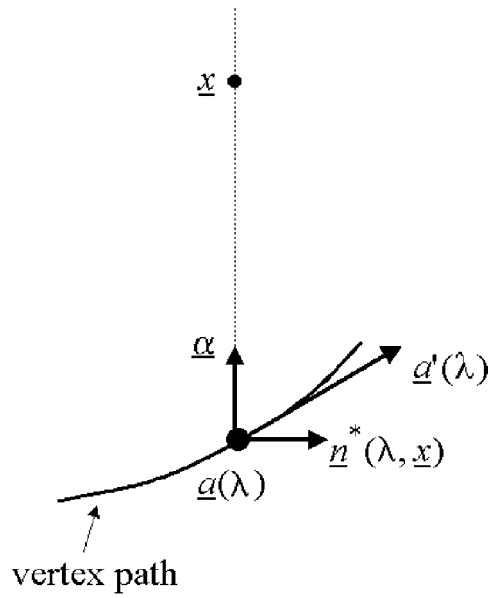


**Figure 4.** Definition of  $\underline{n}^*(\lambda, \underline{x})$ . The vector  $\underline{n}^*(\lambda, \underline{x})$  is the unit vector orthogonal to the line connecting  $\underline{x}$  to  $\underline{a}(\lambda)$ , with orientation such that  $\underline{a}'(\lambda) \cdot \underline{n}^*(\lambda, \underline{x}) > 0$ .

$\underline{n}^*(\lambda, \underline{x})$  is the unit vector that is orthogonal to the line connecting  $\underline{a}(\lambda)$  to  $\underline{x}$  with sign chosen so that  $\underline{a}'(\lambda) \cdot \underline{n}^*(\lambda, \underline{x}) > 0$  as shown in figure 4. Mathematically,

$$\underline{n}^*(\lambda, \underline{x}) = \frac{\underline{a}'(\lambda) - (\underline{a}'(\lambda) \cdot \underline{\alpha})\underline{\alpha}}{\|\underline{a}'(\lambda) - (\underline{a}'(\lambda) \cdot \underline{\alpha})\underline{\alpha}\|} \quad (27)$$

with  $\underline{\alpha} = (\underline{x} - \underline{a}(\lambda)) / \|\underline{x} - \underline{a}(\lambda)\|$ . Condition 2 ensures that  $\underline{\alpha}$  and  $\underline{a}'(\lambda)$  are not collinear, so the denominator of (27) never vanishes and  $\underline{a}'(\lambda) \cdot \underline{n}^*(\lambda, \underline{x})$  is always non-zero. Geometrically,  $\underline{n}^*$  selects the correct value of the filtered projection  $g_F$  for backprojection through  $\underline{x}$ .

Now, the definition of  $w(\lambda, \underline{n})$  is given. Physically,  $w(\lambda, \underline{n})$  is a weight used to account for information redundancy in the dataset; it plays the same role as the weight used in standard short-scan FBP (Parker *et al* 1982). According to formulae (2) and (14), fan-beam projections provide identical information for the reconstruction of  $f$  at  $\underline{x}$  when their vertices form a line containing  $\underline{x}$ . Indeed, for each vertex point on a line orthogonal to a given direction  $\underline{n}$  and passing through  $\underline{x}$ ,  $\underline{a}(\lambda) \cdot \underline{n} = \underline{x} \cdot \underline{n}$  and  $g_F(\lambda, \underline{n}) / (2\pi \underline{a}'(\lambda) \cdot \underline{n}) = p_F(\underline{n}, \underline{x} \cdot \underline{n})$ . The weight  $w(\lambda, \underline{n})$  accounts for this redundancy. Let  $N(\underline{n}, s)$  be the number of intersections of the line  $(\underline{n}, s)$  with the vertex path. For lines through the ROI,  $N(\underline{n}, s) \geq 1$  and for any such fixed line, the intersections are labelled  $\underline{a}(\lambda_i)$ ,  $i = 1, \dots, N(\underline{n}, s)$ . The dependence of  $\lambda_i$  on the line will be denoted as  $\lambda_i(\underline{n}, s)$  when required. For each line through the ROI, a weighting function  $\hat{w}_{(\underline{n}, s)}$  is defined such that

$$\sum_{i=1}^{N(\underline{n}, s)} \hat{w}_{(\underline{n}, s)}(\lambda_i) = 1. \quad (28)$$

Expressed in terms of weights on projection values  $w(\lambda, \underline{n}) = \hat{w}_{(\underline{n}, \underline{a}(\lambda) \cdot \underline{n})}(\lambda)$ .

The simplest weighting function satisfying (28) is  $w(\lambda, \underline{n}) = 1/N(\underline{n}, \underline{a}(\lambda) \cdot \underline{n})$ . In practice, however, this choice may introduce discretization errors in the reconstruction because  $N(\underline{n}, s)$  is in general a discontinuous function. The following formula provides a smooth definition

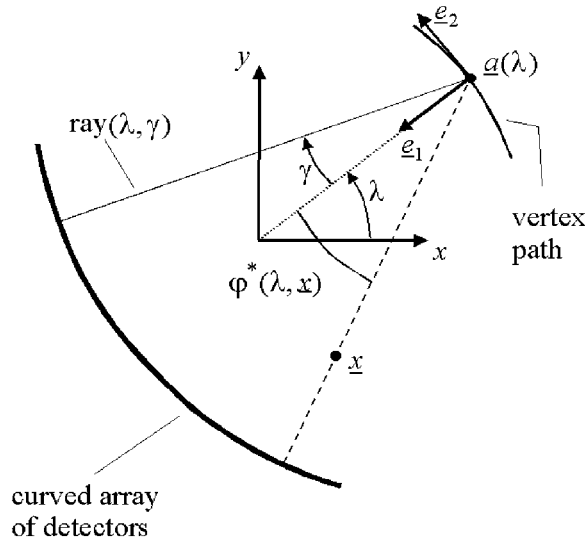


Figure 5. Fan-beam geometry with equi-angular rays.

of  $w(\lambda, \underline{n})$  that is better suited for numerical implementation, although it implies uneven weighting between equal contributions,

$$w(\lambda, \underline{n}) = \frac{c(\lambda)}{\sum_{i=1}^{N(\underline{n}, \underline{a}(\lambda))} c(\lambda_i(\underline{n}, \underline{a}(\lambda) \cdot \underline{n}))} \quad (29)$$

where  $c(\lambda)$  is a smooth positive function which vanishes at the endpoints of each segment composing the vertex path. Note that the numerator of (29) always appears as one of the terms in the denominator.

### 5. Specific geometries

This section shows how to apply the FBP reconstruction formula (26) when the fan-beam projections are measured using equi-angular rays or equally spaced collinear detectors. To simplify the discussion, the motion of  $\underline{a}(\lambda)$  is restricted to be on a circle of radius  $R_o$  and centre  $\underline{x} = 0$ , with the object confined to the region  $\|\underline{x}\| < R_m < R_o$ . The vertex path is parametrized using the polar angle. So,  $\underline{a}(\lambda) = R_o(\cos \lambda, \sin \lambda)$ , with  $\lambda \in \Lambda \subset [0, 2\pi)$ , and  $\underline{a}'(\lambda) = R_o(-\sin \lambda, \cos \lambda)$ . The fan-beam projections are non-truncated.

#### 5.1. Equi-angular rays

The data acquisition geometry is illustrated in figure 5. The ray sums in a given fan-beam projection are parametrized by the angle  $\gamma$  between the rays and the line connecting  $\underline{a}(\lambda)$  to the origin  $\underline{x} = 0$ . The notation  $g^{(m)}(\lambda, \gamma)$  is used to describe the measured fan-beam projection, with  $\gamma \in [-\gamma_m, \gamma_m]$  where  $\gamma_m$  is the half fan-angle. By definition,

$$g^{(m)}(\lambda, \gamma) = g(\lambda, \underline{\alpha}(\gamma)) \quad (30)$$

with  $\underline{\alpha} = \cos \gamma \underline{e}_1 + \sin \gamma \underline{e}_2$  using the unit orthogonal vectors  $\underline{e}_1 = -\underline{a}(\lambda)/\|\underline{a}(\lambda)\| = -(\cos \lambda, \sin \lambda)$  and  $\underline{e}_2 = \underline{a}'(\lambda)/\|\underline{a}'(\lambda)\| = (-\sin \lambda, \cos \lambda)$  (see figure 5). Conversely,

$$g(\lambda, \underline{\alpha}) = g^{(m)}(\lambda, \gamma(\lambda, \underline{\alpha})) \quad (31)$$

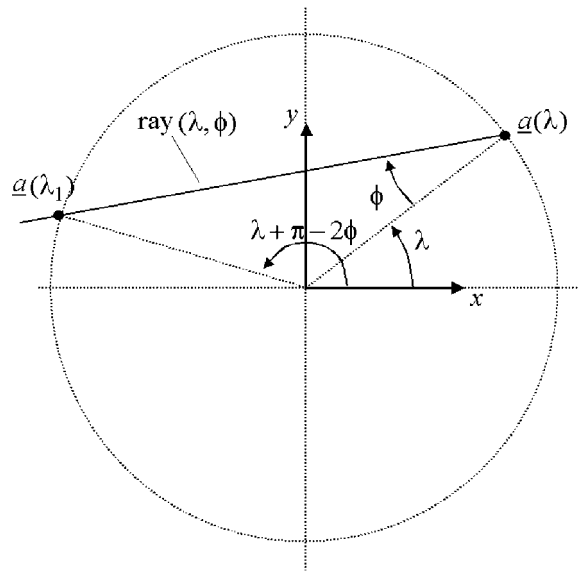


**Figure 6.** Possible intersection  $a(\lambda_1)$  between the vertex path and the ray  $(\lambda, \phi)$  in fan-beam geometry with vertex points on a circle and equi-angular rays. The intersection, if any, is at the angle  $\lambda_1 = \lambda + \pi - 2\phi$ .

with

$$\gamma(\lambda, \underline{x}) = \arctan \frac{\underline{x} \cdot \underline{e}_2}{\underline{x} \cdot \underline{e}_1} \quad |\gamma(\lambda, \underline{x})| < \pi/2. \quad (32)$$

As shown in appendix C, the FBP reconstruction formula using  $g^{(m)}(\lambda, \gamma)$  takes the form

$$f(\underline{x}) = \frac{1}{2\pi} \int_{\Lambda} d\lambda \frac{1}{\|\underline{x} - \underline{a}(\lambda)\|} \left[ w(\lambda, \phi) g_F^{(m)}(\lambda, \phi) \right]_{\phi=\phi^*(\lambda, \underline{x})} \quad (33)$$

where  $\phi^*(\lambda, \underline{x})$  is the angle characterizing the ray that diverges from  $\underline{a}(\lambda)$  and contains  $\underline{x}$ , and

$$g_F^{(m)}(\lambda, \phi) = \int_{-\gamma_m}^{\gamma_m} d\gamma h_H(\sin(\phi - \gamma)) \left( \frac{\partial}{\partial \lambda} + \frac{\partial}{\partial \gamma} \right) g_m(\lambda, \gamma). \quad (34)$$

By definition,  $\underline{x} - \underline{a}(\lambda)$  is along  $\cos \phi^* \underline{e}_1 + \sin \phi^* \underline{e}_2$  (see figure 5). Therefore,

$$\phi^*(\lambda, \underline{x}) = \arctan \frac{\underline{x} \cdot \underline{e}_2}{R_o + \underline{x} \cdot \underline{e}_1} \quad |\phi^*(\lambda, \underline{x})| < \pi/2. \quad (35)$$

In this particular case where the motion of the vertex point is restricted to being on a circle, a simplified expression can be given for the weighting function  $w$ . Following the discussion in section 4.2, let  $c(\lambda)$  be a smooth function that vanishes at the extremities of each arc composing the vertex path. Define  $c(\lambda)$  to be zero when  $\lambda \notin \Lambda \cap [0, 2\pi)$ , and  $c(\lambda)$  to be  $c(\lambda - 2\pi)$  when  $\lambda$  is larger than  $2\pi$ . With this definition,

$$w(\lambda, \phi) = \frac{c(\lambda)}{c(\lambda) + c(\lambda + \pi - 2\phi)} \quad (36)$$

because the ray  $(\lambda, \phi)$  can only hit the circle twice, once at  $\lambda$  and once at  $\lambda + \pi - 2\phi$ . See figure 6.

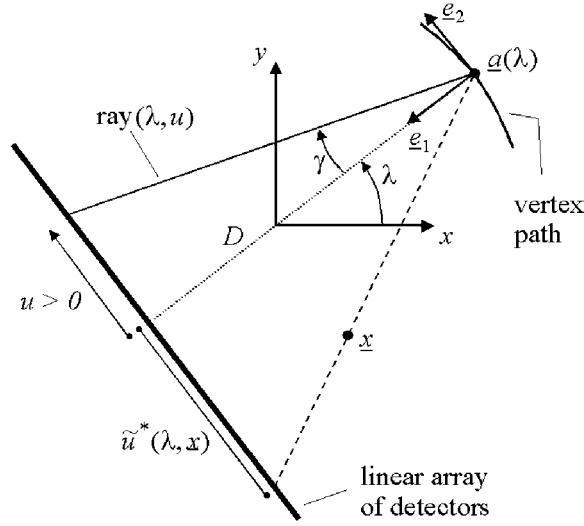


Figure 7. Fan-beam geometry with equally spaced collinear detectors.

### 5.2. Equally spaced collinear detectors

The data acquisition geometry is illustrated in figure 7. This time, the fan-beam projections are measured using a linear array of detectors parallel to  $a'(\lambda)$  and at a distance  $D$  from  $a(\lambda)$ . The position of each detector in the array is given by a signed distance  $u$  increasing in the direction of  $e_2 = a'(\lambda)/\|a'(\lambda)\|$  and such that  $u = 0$  corresponds to the orthogonal projection of  $a(\lambda)$  onto the detector array. The notation  $g^{(m)}(\lambda, u)$  is used to denote the measured projections.

Geometrically, the ray  $(\lambda, u)$  is identical to the ray  $(\lambda, \gamma)$  of figure 5 with  $u = D \tan \gamma$ . Therefore, a reconstruction formula for  $f(x)$  from  $g^{(m)}(\lambda, u)$  is conveniently obtained by applying the changes of variable  $u = D \tan \gamma$  and  $\tilde{u} = D \tan \phi$  in equations (33) and (34). The result is

$$f(x) = \frac{1}{2\pi} \int_{\Lambda} d\lambda \frac{1}{R_o + \underline{x} \cdot e_1} \left[ w(\lambda, \tilde{u}) g_F^{(m)}(\lambda, \tilde{u}) \right]_{\tilde{u}=\tilde{u}^*(\lambda, \underline{x})} \quad (37)$$

with

$$g_F^{(m)}(\lambda, \tilde{u}) = \int_{-u_m}^{u_m} du h_H(\tilde{u} - u) \frac{D}{\sqrt{D^2 + u^2}} \left( \frac{\partial}{\partial \lambda} + \frac{D^2 + u^2}{D} \frac{\partial}{\partial u} \right) g^{(m)}(\lambda, u) \quad (38)$$

where  $u_m = D \tan \gamma_m$ ,

$$\tilde{u}^*(\lambda, \underline{x}) = D \tan \phi^*(\lambda, \underline{x}) = \frac{D \underline{x} \cdot e_2}{R_o + \underline{x} \cdot e_1} \quad (39)$$

is the detector location of the line connecting  $\underline{x}$  to  $a(\lambda)$  (see equation (35) and figure 7), and

$$w(\lambda, \tilde{u}) = \frac{c(\lambda)}{c(\lambda) + c(\lambda + \pi - 2 \arctan(\tilde{u}/D))} \quad (40)$$

with  $c(\lambda)$  defined as in section 5.1.

The following relations were used to obtain the above equations

$$\sin(\phi - \gamma) = \frac{D}{\sqrt{D^2 + \tilde{u}^2}\sqrt{D^2 + u^2}}(\tilde{u} - u) \quad (41)$$

$$h_H(\sin(\phi - \gamma)) = \frac{\sqrt{D^2 + \tilde{u}^2}\sqrt{D^2 + u^2}}{D}h_H(\tilde{u} - u) \quad (42)$$

and

$$\frac{1}{\|\underline{x} - \underline{a}(\lambda)\|} \frac{\sqrt{D^2 + (\tilde{u}^*)^2}}{D} = \frac{1}{\cos \phi^* \|\underline{x} - \underline{a}(\lambda)\|} = \frac{1}{R_o + \underline{x} \cdot \underline{e}_1}. \quad (43)$$

## 6. Simulations and results

The FBP formula (37) for equally spaced collinear detectors was evaluated using computer-simulated data of a 3D head phantom designed by Schaller (1998). For the simulations, the vertex path was always lying in the plane  $z = 0$ . All displayed images thus correspond to the slice  $z = 0$  through the phantom.

The 3D head phantom of Schaller (1998) is built from ellipsoids, elliptical cylinders and cones of intensity ranging between 0 for the nose and 1.8 for the skull. Fine structures appear in the compressed window of intensities between 1.0 and 1.1. The half lengths of the skull are 96 mm and 120 mm.

### 6.1. Vertex paths

Simulations were performed for five different vertex paths on the circle of radius  $R_o = 270$  mm and centre  $\underline{x} = 0$ . Note that the selected value of  $R_o$  is about half that of CT scanners. This choice was made so that the fan-angle for the head phantom is comparable to the maximum fan-angle for CT scanners (with  $R_o = 270$  mm and  $R_m = 125$ ,  $\gamma_m = 27.6^\circ$ ).

The vertex paths were described using the polar angle  $\lambda$ , so that  $\underline{a}(\lambda) = R_o(\cos \lambda, \sin \lambda)$ . The first vertex path was the full circle. The second vertex path was a conventional short-scan defined with  $\lambda \in [-\gamma_m, \pi + \gamma_m]$ . The third vertex path was the half circle  $\lambda \in [0, \pi]$ . The fourth vertex path was an arc of length  $160^\circ$  centred on the point  $\lambda = \pi/2$ .

The fifth vertex path was the union of three arcs as shown in figure 1(d). The centre of the arcs were at  $\lambda = 60, 180$  and  $300^\circ$ , and the length of each arc was  $80^\circ$ . With these values, the radius of the largest disc inside the triangular ROI was about 47 mm. See figure 1 for an illustration of the last four paths.

### 6.2. Data sampling and implementation details

For each path, the projections were sampled at a rate  $\Delta\lambda = 2\pi/1024$ , with 512 ray sums per projection for a field-of-view (FOV) of radius  $R_m = 125$  mm (i.e.  $\Delta u = 0.55$  mm for a source-detector distance  $D = R_o = 270$  mm). The line integrals were computed using analytical formulae. For simulation with noise, Poisson noise was added to the noise-free data so as to simulate a *total* number of counts of  $5 \times 10^{10}$  for each data acquisition geometry.

The reconstructions were always achieved on a grid of  $512 \times 512$  square pixels covering the entire FOV with a pixel size of 0.55 mm, even though some paths provide only enough information for accurate reconstruction in a subset of the FOV.

The Hilbert transform was applied in the Fourier domain using the apodization window of Hanning at Nyquist frequency, and the derivatives with respect to  $\lambda$  and  $u$  were implemented using the 2-point formulae

$$\frac{\partial}{\partial \lambda} g^{(m)}(\lambda, u) \simeq \frac{g^{(m)}(\lambda + \Delta\lambda, u) - g^{(m)}(\lambda - \Delta\lambda, u)}{2\Delta\lambda} \quad (44)$$

$$\frac{\partial}{\partial u} g^{(m)}(\lambda, u) \simeq \frac{g^{(m)}(\lambda, u + \Delta u) - g^{(m)}(\lambda, u - \Delta u)}{2\Delta u}. \quad (45)$$

The function  $c(\lambda)$  used to handle data redundancy through the function  $w(\lambda, \tilde{u})$  of equation (40) was defined as follows. For the full circle,  $w(\lambda, \tilde{u}) = 1/2$ . For the short-scan, the half-circle, the  $160^\circ$  arc, and for each segment of the fifth path,

$$c(\lambda) = \begin{cases} \cos^2 \frac{\pi(\lambda - \lambda_s - d)}{2d} & \text{if } \lambda_s < \lambda < \lambda_s + d \\ 1 & \text{if } \lambda_s + d < \lambda < \lambda_e - d \\ \cos^2 \frac{\pi(\lambda - \lambda_e + d)}{2d} & \text{if } \lambda_e - d < \lambda < \lambda_e \end{cases} \quad (46)$$

where  $\lambda_s$  and  $\lambda_e$  are the starting and ending points of the scan or scan segment respectively, and  $d$  is an angular interval over which  $c(\lambda)$  smoothly drops from 1 to 0. The value  $d = 10^\circ$  was used.

The backprojection step was implemented using a voxel-driven approach with linear interpolation of the filtered data.

### 6.3. Results

Figures 8(a), (c) and (d) show the reconstructions obtained with the new algorithm (formula (37)) using the half-circle, the three-segment path, and the  $160^\circ$  arc, respectively. Figure 8(b) shows a reconstruction obtained by attempting to apply pre-existing theory: a Parker-like weighting was first applied to the data to account for ray redundancy over  $180^\circ$ , then reconstruction was achieved with 1D ramp filtering and conventional fan-beam backprojection. Figure 8(b) exhibits significant artefacts at the compressed greyscale window of [1.0, 1.1], while figures 8(a), (c) and (d) only exhibit faint streak artifacts due to finite sampling and discretization effects.

To appreciate the accuracy of the reconstructions in figures 8(a), (c) and (d), reconstructions were also performed for a full scan and a conventional short scan, using both the new algorithm (formula (37)) and the standard fan-beam convolution-backprojection method (with Parker weighting in the short scan case). The results are displayed in figure 9. Within their respective ROI, the reconstructions of figures 8(a), (c) and (d) appear as accurate as the full scan and short scan reconstructions. Up to small differences in discretization effects, the reconstructions obtained with the new algorithm (equation (37)) are similar to those provided with the conventional algorithms. The small differences are attributed to the unmatched frequency apodization in the filtering steps.

Figure 10 shows results with noisy data. The reconstructions obtained with the new algorithm (equation (37)) for the full scan (figure 10(a)) and the half-circle (figure 10(c)) are compared with those obtained for the same paths using conventional fan-beam backprojection with 1D ramp-filtering and Parker-like weighting when needed (figures 10(b), (d)). These results demonstrate that the new algorithm has noise properties similar to those of conventional fan-beam FBP, which was expected because the stability of the derivative and Hilbert filters in the new method is similar to that of the ramp filter. The slight differences observed between

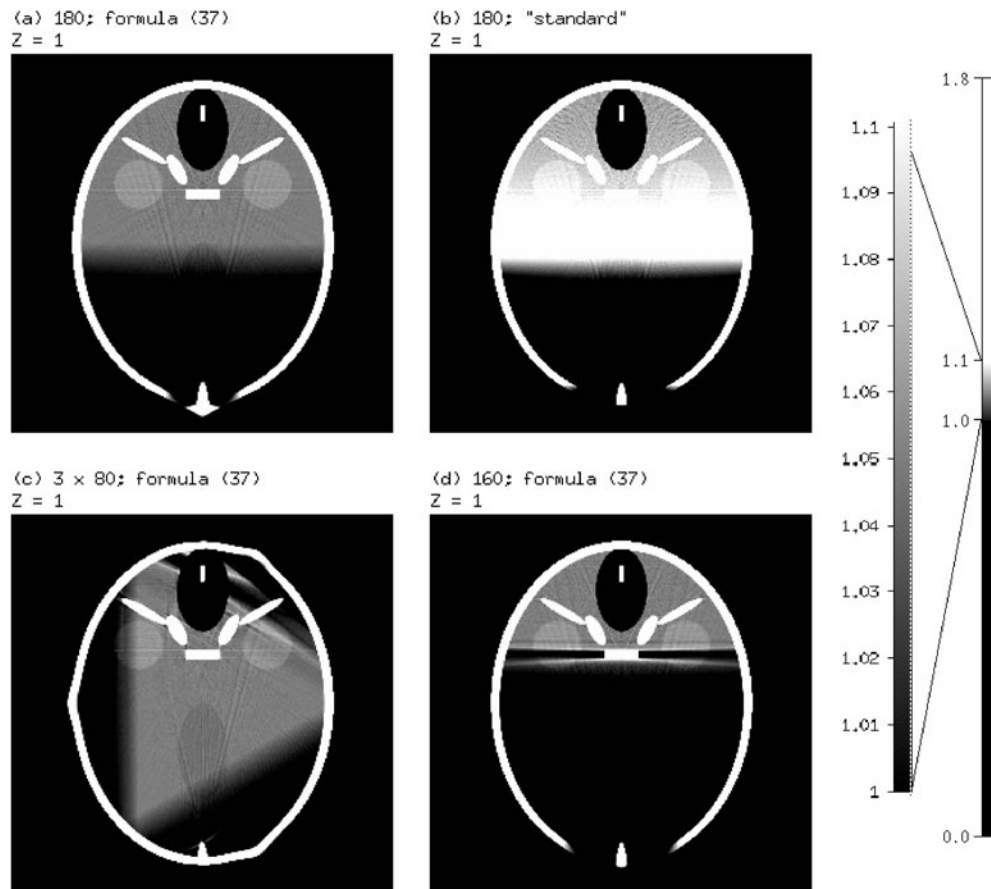


**Figure 8.** Top row: reconstruction from data on a half circle ( $180^\circ$ ), using (a) the new algorithm (formula (37)) and (b) the conventional short-scan algorithm, modified for  $180^\circ$ ; the poor quality of image (b) indicates inadequacy of preexisting theory. Bottom row: reconstruction from data on (c) a union of three arcs of length  $80^\circ$  and (d) an arc of  $160^\circ$ , using the new algorithm (formula (37)). All images are displayed using a highly compressed greyscale window focusing on fine structures in the phantom.

figures 10(a) and (b) are attributed to the difficulty in exactly matching the apodization of the filters in the two algorithms, but an analysis of the trade-off between noise and spatial resolution would be needed to confirm this point.

Figure 10 also shows that little differences in noise properties occur when reconstructing from fan-beam data on a half-circle instead of a full circle, which demonstrates a good robustness of the new algorithm (compare figures 10(a) and (c)).

## 7. Discussion and conclusions

A new result in 2D image reconstruction has been presented: improved conditions on the measurements required for reconstruction of an ROI can be expressed in terms of fan-beam projections. Each ray through the ROI must lie in a complete (non-truncated) fan-beam projection measurement. New algorithms have been proposed which allow the exact reconstruction of an ROI from complete fan-beam projections acquired when this

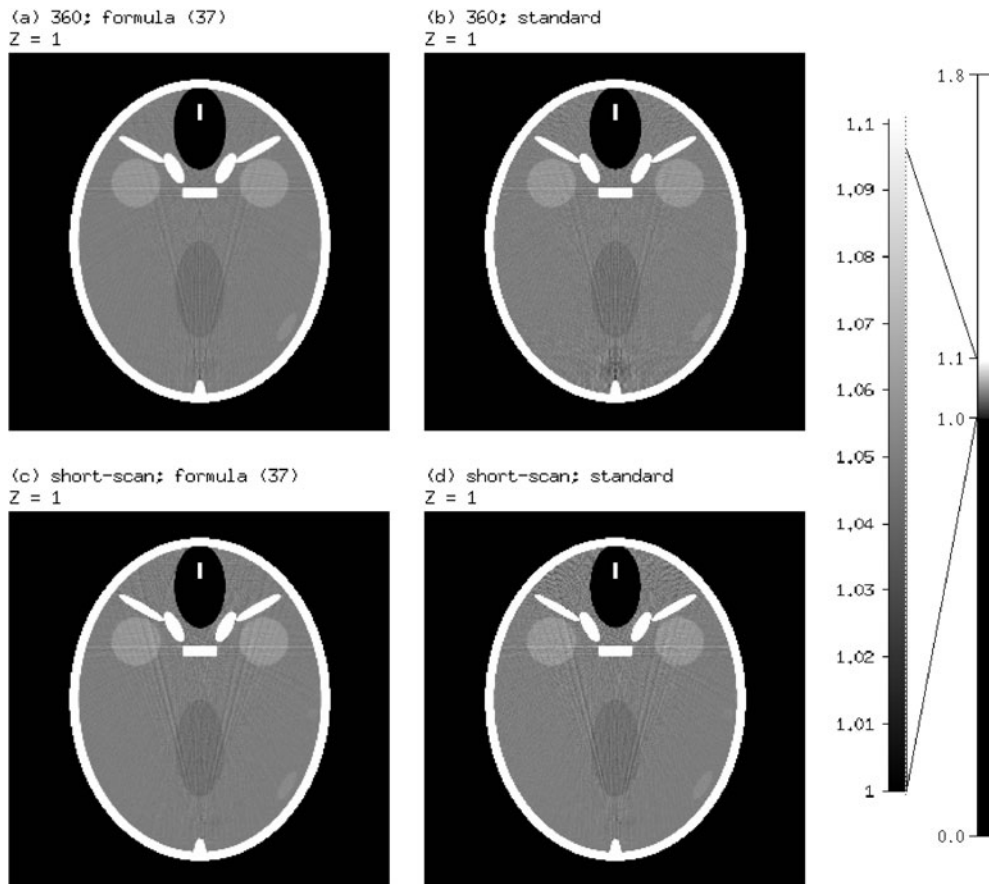


**Figure 9.** Top row: reconstruction from data over  $360^\circ$ , using (a) the new algorithm (formula (37)) and (b) conventional backprojection and 1D filtering. Bottom row: reconstruction from short-scan data ( $240^\circ$ ) using (c) the new algorithm (formula (37)) and (d) the conventional short-scan algorithm (backprojection, 1D ramp filtering and Parker weighting). All images are displayed using a highly compressed greyscale window focusing on fine structures in the phantom.

condition is satisfied. These algorithms are straightforward to implement and involve only familiar image processing operators, namely differentiation, Hilbert filtering, and fan-beam backprojection. For circular trajectories, FBP formulations have been derived for curved-detector and flat-detector projections lying on less than a short-scan. These formulations differ from conventional FBP in that projections are not processed individually but in pairs to allow the computation of a derivative along the source path.

Most papers and textbooks on 2D tomography with limited data have focused on subjects such as the interior, exterior, and limited-angle problems, where stability and unicity never hold simultaneously. Common wisdom therefore assumes that the exact and stable 2D reconstruction of an object is possible only when all line integrals through the object are measured. This assumption is usually explained by the non-local character of the well-known ramp filter. In contrast, it has long been known that exact and stable 3D ROI reconstruction is possible from non-truncated cone-beam projections provided that the *local* Tuy condition (Tuy 1983) is satisfied (any plane passing through a neighbourhood of the ROI must intersect the path of the x-ray source). However, the implications of these 3D results for 2D tomography

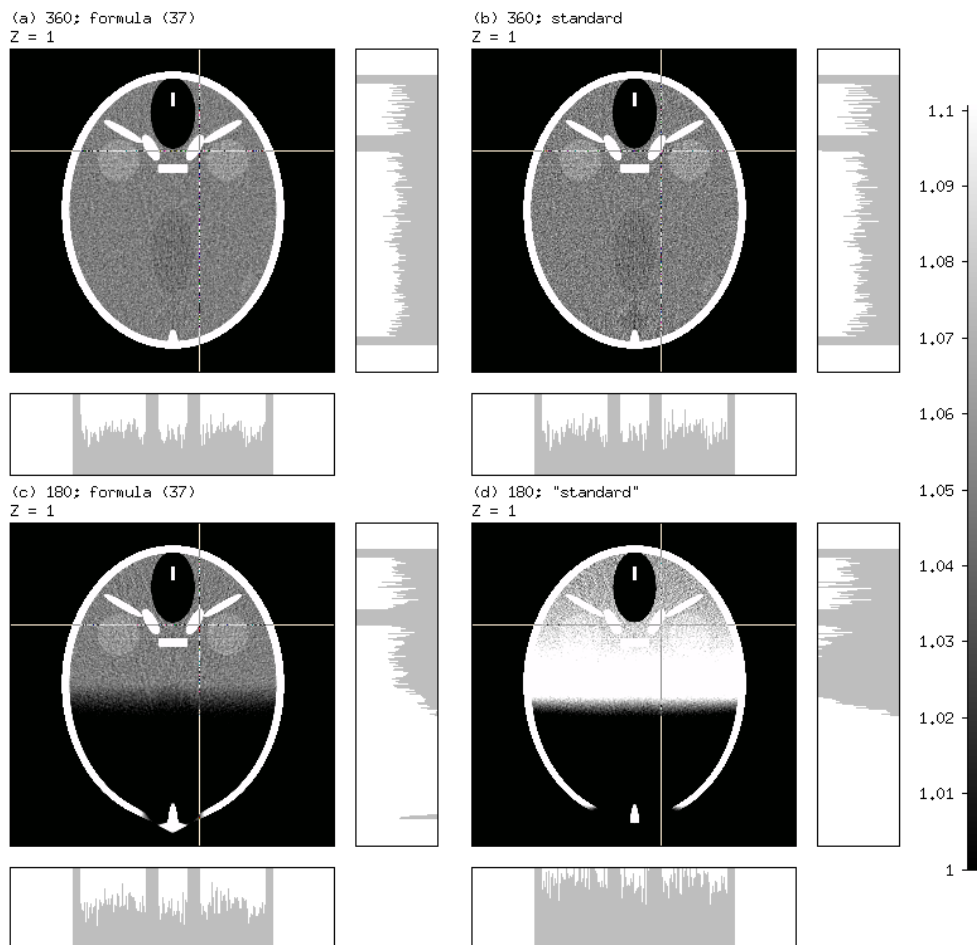


**Figure 10.** Reconstructions with Poisson noise added to the data (a total number of  $(5 \times 10^{10})$  counts were simulated for each data acquisition geometry). Top row: reconstruction from data over  $360^\circ$ , using (a) the new algorithm (formula (37)) and (b) conventional FBP. Bottom row: reconstruction from a half circle of data ( $180^\circ$ ) using (c) the new algorithm (formula (37)) and (d) the conventional short-scan algorithm, modified for a half circle. All images are displayed using a highly compressed greyscale window focusing on the fine structures in the phantom.

have never, to the best of our knowledge, been investigated, even though the main ingredient, equation (10), was published as early as in 1980 for the  $n$ -dimensional problem. Apart from this old result, the present work has been inspired by the 3D reconstruction algorithm recently proposed by Katsevich (2002) for spiral cone-beam CT. The sufficient condition for reconstruction of a 2D ROI from non-truncated fan-beam projections simply translates into two dimensions the *local* Tuy condition: the path followed by the x-ray source must have an intersection with any line passing through a neighbourhood of the ROI. This condition is much less restrictive than the standard condition used to define a short-scan acquisition in CT, namely that the short-scan vertex path should intersect any line crossing the support of the whole object, even if only part of the object is to be reconstructed.

The simulations presented in this paper have demonstrated that ROI fan-beam reconstruction is highly accurate, with discretization artefacts comparable to those of

conventional full-scan ( $360^\circ$  scan) fan-beam tomography. The spatial resolution appears slightly lower than for conventional FBP reconstruction, but the noise is also slightly lower. These differences are thought to be related to the difficulty in perfectly matching the frequency apodization of the various operations in the two algorithms.

The practical implications of our results could be significant for all applications of CT where 2D reconstruction is still used. This includes high-resolution 2D step-and-shoot CT, spiral CT with single-row scanners, and also spiral CT with multi-row detectors when the number of rows is small enough to apply approximate algorithms based on 2D reconstruction, such as the advanced single-slice rebinning algorithm (Larson *et al* 1998, Kachelriess *et al* 2000). For instance, improved cardiac imaging could be achieved by decreasing the length of the vertex path well below the length of the standard short-scan segment of  $180^\circ$  plus the fan-angle. With such reduced measurement data, standard fan-beam algorithms would only provide non-quantitative reconstructions. Finally, the new algorithms could also allow quantitative reconstructions for some non-destructive testing applications where so far only local ('lambda') tomography reconstruction of the object discontinuities has been possible.

The main theoretical implication of our results is to alert the community to an open problem in 2D image reconstruction from projections. Given an ROI inside an object, what possible collections of line integral measurements admit accurate reconstruction of the ROI? This paper provides only a partial answer to this question.

### Acknowledgment

The work of F Noo and R Clackdoyle was supported by the National Institutes of Health, grant number R21 CA82843.

### Appendix A

A formal proof of the rebinning formula of equations (10) and (11) can be obtained as follows. First, using equations (11) and (9) and the relation  $h_H(as) = (1/a)h_H(s)$  for any  $a > 0$ , the right-hand side of equation (10) becomes

$$g_H(\lambda, \underline{n}) = - \int_{S^1} d\alpha h_H(\underline{n} \cdot \alpha) g(\lambda, \alpha) = - \int_{S^1} d\alpha \int_0^{+\infty} dt t h_H(\underline{n} \cdot t\alpha) f(\underline{a}(\lambda) + t\alpha). \quad (47)$$

Applying the change of variable  $\underline{x} = \underline{a}(\lambda) + t\alpha$ , which is equivalent to a change of variable from polar coordinates to Cartesian coordinates in  $\mathbb{R}^2$ , equation (47) becomes

$$g_H(\lambda, \underline{n}) = - \int_{\mathbb{R}^2} d\underline{x} f(\underline{x}) h_H(\underline{n} \cdot (\underline{x} - \underline{a}(\lambda))). \quad (48)$$

Now,  $h_H(\underline{n} \cdot (\underline{x} - \underline{a}(\lambda)))$  can be written as

$$\int_{\mathbb{R}} ds' \delta(\underline{n} \cdot \underline{x} - s') h_H(s' - \underline{n} \cdot \underline{a}(\lambda)) \quad (49)$$

and, using  $h_H(-s) = -h_H(s)$ , equation (48) yields

$$\begin{aligned} g_H(\lambda, \underline{n}) &= \int_{\mathbb{R}^2} d\underline{x} f(\underline{x}) \int_{\mathbb{R}} ds' \delta(\underline{x} \cdot \underline{n} - s') h_H(\underline{a}(\lambda) \cdot \underline{n} - s') \\ &= \int_{\mathbb{R}} ds' h_H(\underline{a}(\lambda) \cdot \underline{n} - s') \int_{\mathbb{R}^2} d\underline{x} f(\underline{x}) \delta(\underline{x} \cdot \underline{n} - s') \\ &= \int_{\mathbb{R}} ds' h_H(\underline{a}(\lambda) \cdot \underline{n} - s') p(\underline{n}, s') \end{aligned} \quad (50)$$

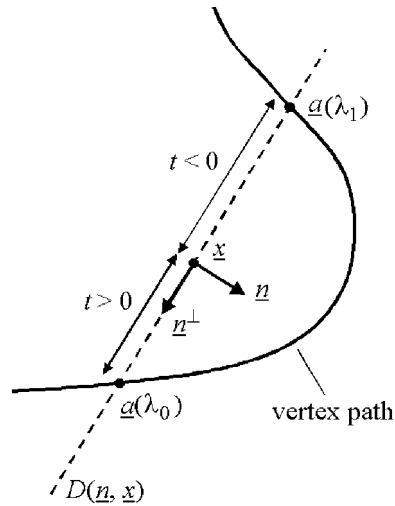


**Figure 11.** Illustration of the intersections of the vertex path with a line passing through a given  $\underline{x}$ . In this figure, the line is orthogonal to  $\underline{n}$  and hits the vertex path at two locations  $\underline{a}(\lambda_0)$  and  $\underline{a}(\lambda_1)$ . The intersections are specified by a signed distance  $t$  from  $\underline{x}$ .

where the definition of the Radon transform given by equation (1) was applied. Finally, substituting  $s = \underline{a}(\lambda) \cdot \underline{n}$  in the above and using equation (6) gives  $g_H(\lambda, \underline{n}) = p_H(\underline{n}, s)$  with  $s = \underline{a}(\lambda) \cdot \underline{n}$ .

## Appendix B

The proof of the FBP formula (26) is as follows. Consider a fixed direction  $\underline{n} = (-\sin \phi, \cos \phi)$  and denote by  $\mathcal{D}(\underline{n}, \underline{x})$  the line of direction  $\underline{n}^\perp = (\cos \phi, \sin \phi)$  passing through  $\underline{x}$ . Any vertex  $\underline{a}(\lambda)$  belonging to the line  $\mathcal{D}(\underline{n}, \underline{x})$  is such that

$$\underline{x} + t\underline{n}^\perp = \underline{a}(\lambda) \quad (51)$$

for some positive or negative value of  $t$  (see figure 11). Clearly,  $|t| = \|\underline{x} - \underline{a}(\lambda)\|$ . For any fixed point  $\underline{x}$ , relation (51) with  $t$  viewed as a function of  $\lambda$  defines a change of variable between  $\phi$  and  $\lambda$ . Differentiating each side of this equation with respect to  $\lambda$  yields

$$\frac{dt}{d\lambda} \underline{n}^\perp + t\underline{n} \frac{d\phi}{d\lambda} = \underline{a}'(\lambda). \quad (52)$$

So,

$$\underline{a}'(\lambda) \cdot \underline{n} = t \frac{d\phi}{d\lambda} \quad \text{and} \quad \left| \frac{d\phi}{d\lambda} \right| = \frac{|\underline{a}'(\lambda) \cdot \underline{n}|}{\|\underline{x} - \underline{a}(\lambda)\|} \quad (53)$$

for any vertex  $\underline{a}(\lambda) \in \mathcal{D}(\underline{n}, \underline{x})$ . The use of this result with the rebinning formula (14) leads to

$$\begin{aligned} \left| \frac{d\phi}{d\lambda} \right| p_F(\underline{n}, \underline{a}(\lambda) \cdot \underline{n}) &= \frac{1}{2\pi \|\underline{x} - \underline{a}(\lambda)\|} \text{sign}(\underline{a}'(\lambda) \cdot \underline{n}) g_F(\lambda, \underline{n}) \\ &= \frac{1}{2\pi \|\underline{x} - \underline{a}(\lambda)\|} g_F(\lambda, \underline{\beta}) \end{aligned} \quad (54)$$

with  $\underline{\beta} = \text{sign}(\underline{a}'(\lambda) \cdot \underline{n})\underline{n}$ , since  $g_F(\lambda, -\underline{n}) = -g_F(\lambda, \underline{n})$  for any unit vector (see equation (15)). Now, it is shown that  $\underline{\beta}$  is equal to the vector  $\underline{n}^*(\lambda, \underline{x})$  given by equation (27).

Since  $\underline{n}^*(\lambda, \underline{x}) \cdot \underline{\alpha} = 0$  and  $\underline{\alpha}$  is orthogonal to  $\underline{n}$ , the unit vectors  $\underline{n}$  and  $\underline{n}^*(\lambda, \underline{x})$  must be parallel and thus

$$\underline{n}^*(\lambda, \underline{x}) = \text{sign}(\underline{n}^* \cdot \underline{n})\underline{n} = \text{sign}(\underline{a}'(\lambda) \cdot \underline{n})\underline{n} = \underline{\beta}. \quad (55)$$

Finally, by equation (51),  $\underline{a}(\lambda) \cdot \underline{n} = \underline{x} \cdot \underline{n}$ ; therefore

$$\left| \frac{d\phi}{d\lambda} \right| p_F(\underline{n}, \underline{x} \cdot \underline{n}) = \frac{1}{2\pi \|\underline{x} - \underline{a}(\lambda)\|} g_F(\lambda, \underline{n}^*(\lambda, \underline{x})) \quad (56)$$

for any  $\underline{a}(\lambda) \in \mathcal{D}(\underline{n}, \underline{x})$ . A direct change of variable from  $\phi$  to  $\lambda$  in the parallel-beam reconstruction formula (2) with  $|d\phi/d\lambda| p_F(\underline{n}, \underline{x} \cdot \underline{n})$  given by the above equation leads to equation (26), with weighting  $w(\lambda, \underline{n})$  to properly account for each intersection of  $\mathcal{D}(\underline{n}, \underline{x})$  with the vertex path (see section 4.2 for the definition of  $w(\lambda, \underline{n})$ ).

## Appendix C

To prove formula (33) with  $g_F^{(m)}$  given by (34), it is only necessary to show that

$$g_F^{(m)}(\lambda, \phi) \Big|_{\phi=\phi^*(\lambda, \underline{x})} = g_F(\lambda, \underline{n}) \Big|_{\underline{n}=\underline{n}^*(\lambda, \underline{x})} \quad (57)$$

with  $g_F$  given by equations (15) and (16), and  $\underline{n}^*(\lambda, \underline{x})$  given by (27). Compare (26) with (33).

First, using the parametrization

$$\underline{n} = \underline{n}(\phi) = -\sin \phi \underline{e}_1 + \cos \phi \underline{e}_2 \quad (58)$$

suggested in (12),

$$g_F(\lambda, \underline{n}(\phi)) = \int_{-\gamma_m}^{\gamma_m} d\gamma h_H(\sin(\phi - \gamma)) g'(\lambda, \underline{\alpha}(\gamma)) \quad (59)$$

as was observed in section 3.1. Next, recall from formula (16) that  $g'(\lambda, \underline{\alpha})$  is the derivative of  $g(\lambda, \underline{\alpha})$  with respect to  $\lambda$  at fixed direction  $\underline{\alpha}$ . An application of the chain rule in (31) yields

$$g' = \frac{\partial g^{(m)}}{\partial \lambda} + \frac{\partial g^{(m)}}{\partial \gamma} \cdot \frac{\partial \gamma}{\partial \lambda} \quad (60)$$

where, according to (32),

$$\frac{\partial \gamma}{\partial \lambda} = \frac{\partial}{\partial \lambda} \left( \arctan \frac{\underline{\alpha} \cdot \underline{e}_2}{\underline{\alpha} \cdot \underline{e}_1} \right) = 1 \quad (61)$$

because  $d\underline{e}_1/d\lambda = -\underline{e}_2$  and  $d\underline{e}_2/d\lambda = \underline{e}_1$ . Hence,

$$g'(\lambda, \underline{\alpha}(\gamma)) = \left( \frac{\partial}{\partial \lambda} + \frac{\partial}{\partial \gamma} \right) g^{(m)}(\lambda, \gamma) \quad (62)$$

and from (59)

$$g_F(\lambda, \underline{n}(\phi)) = \int_{-\gamma_m}^{\gamma_m} d\gamma h_H(\sin(\phi - \gamma)) \left( \frac{\partial}{\partial \lambda} + \frac{\partial}{\partial \gamma} \right) g^{(m)}(\lambda, \gamma) = g_F^{(m)}(\lambda, \phi). \quad (63)$$

Now, it only remains to be shown that  $\phi^*(\lambda, \underline{x})$  is such that  $\underline{n}(\phi^*(\lambda, \underline{x})) = \underline{n}^*(\lambda, \underline{x})$ , because the application of this relation to (63) yields (57). First, recall from section 5.1 and figure 5 that  $\phi^*(\lambda, \underline{x})$  is the angle characterizing the ray that diverges from  $\underline{a}(\lambda)$  and contains  $\underline{x}$ , so  $\phi^*(\lambda, \underline{x})$  is such that

$$\frac{\underline{x} - \underline{a}(\lambda)}{\|\underline{x} - \underline{a}(\lambda)\|} = \cos \phi^* \underline{e}_1 + \sin \phi^* \underline{e}_2. \quad (64)$$

Next, recall that  $\underline{n}^*(\lambda, \underline{x})$  is given by equation (27) with  $\underline{\alpha} = (\underline{x} - \underline{a}(\lambda))/\|\underline{x} - \underline{a}(\lambda)\|$ . Hence, using  $\cos \phi^* > 0$  and  $\underline{e}_2 = \underline{a}'(\lambda)/\|\underline{a}'(\lambda)\|$ ,

$$\underline{n}^*(\lambda, \underline{x}) = -\sin \phi^* \underline{e}_1 + \cos \phi^* \underline{e}_2. \quad (65)$$

The comparison of (58) and (65) gives the expected result  $\underline{n}(\phi^*(\lambda, \underline{x})) = \underline{n}^*(\lambda, \underline{x})$ .

## References

- Defrise M and Clack R 1994 A cone-beam reconstruction algorithm using shift-variant filtering and cone-beam backprojection *IEEE Trans. Med. Imaging* **13** 186–95
- Grangeat P 1991 Mathematical framework of cone-beam 3D reconstruction via the first derivative of the Radon transform *Mathematical Methods in Tomography (Lecture Notes in Mathematics 1497)* ed G T Herman, A K Louis and F Natterer (Berlin: Springer) pp 66–97
- Hamaker C, Smith K T, Solmon D C and Wagner S L 1980 The divergent beam x-ray transform *Rocky Mountain J. Math.* **10** 253–83
- Kachelriess M, Schaller S and Kalender W 2000 Advanced single-slice rebinning in cone-beam spiral CT *Med. Phys.* **27** 754–72
- Kak A C and Slaney M 1987 *Principles of Computerized Tomography* (Piscataway, NJ: IEEE)
- Katsevich A 2002 Theoretically exact filtered backprojection-type inversion algorithm for spiral CT *SIAM J. Appl. Math.* at press
- Kudo H and Saito T 1994 Derivation and implementation of a cone-beam reconstruction algorithm for non-planar orbits *IEEE Trans. Med. Imaging* **13** 186–95
- Larson G L, Ruth C C and Crawford C R 1998 Nutating slice CT image reconstruction *Patent Application* WO 98/44847
- Natterer F 1986 *The Mathematics of CT* (New York: Wiley)
- Natterer F and Wübbeling F 2001 *Mathematical Methods in Image Reconstruction* (Philadelphia: SIAM)
- Noo F, Clack R and Defrise M 1997 Cone-beam reconstruction from general discrete vertex sets using Radon rebinning algorithms *IEEE Trans. Nucl. Sci.* **44** 1309–16
- Noo F, Defrise M and Clackdoyle R 1999 Single-slice rebinning method for helical cone-beam CT *Phys. Med. Biol.* **44** 561–70
- Parker D L 1982 Optimal short-scan convolution reconstruction for fanbeam CT *Med. Phys.* **9** 254–7
- Schaller S 1998 Practical image reconstruction for cone-beam tomography *PhD Thesis* University of Erlangen
- Tuy H 1983 An inversion formula for cone-beam reconstruction *SIAM J. Appl. Math.* **43** 546–52